ADVANCED ENERGY & SUSTAINABILITY RESEARCH
Open Access
www.advenergysustres.com

Trapa natans Husk-Derived Nanoporous Carbons as Electrode Materials for Sustainable High-Power Microbial Fuel Cell Supercapacitor Systems

Chia-Chieh Hsu, Yi-Chu Lin, Yao-Yu Lin, Hsin-Tien Li, Chung-Sheng Ni, Chao-I Liu, Chao-Chin Chang, Liang-Chen Lin, Yung-Tin Pan, Shih-Fu Liu, Tzu-Yin Liu, and Han-Yi Chen**

Microbial fuel cells (MFCs), which convert chemical energy into electricity using microbes, are an emerging sustainable energy technology. However, high costs and low power output limit the advanced development of MFCs. This study utilizes the agricultural waste, *Trapa natans* husks, to obtain low-cost nanoporous carbons. The *Trapa natans* husk-derived nanoporous carbons (TNHs) are used as electrode materials in *Escherichia coli* system-based MFCs. After optimization of both anode and cathode materials for MFCs, a high average power density of 5713 mW m^{-2} is achieved, which is 1.9 times greater than that of commercial activated carbon. It is shown that TNHs have better bacterial adhesion and electrochemical activities owing to their favorable pore size distribution, suitable functional group, high surface area, and excellent biocompatibility and conductivity. Furthermore, the supercapacitors (SCs) with TNH-based electrodes are utilized to store the energy generated from MFCs. The SC with TNH-600 electrodes exhibits a high specific capacitance of 84 F g^{-1} at a current density of 1 A g^{-1} after 1000 cycles. This study demonstrates that TNH is a promising electrode material for biofriendly and renewable MFCs, and the MFC-SC system with TNH electrodes is a high-power sustainable energy generation and storage device.

1. Introduction

Microbial fuel cells (MFCs) are emerging biotechnologies for environmentally sustainable energy.[1] By converting chemical energy to electricity using microbes, MFCs can be applied to hydrogen production, wastewater treatment, biosensors, and other applications.[2,3] However, its high cost and low power density are two major bottlenecks that need to be resolved.[4] **Figure 1**a shows the basic MFC working principle. The microbes adhering to the anode consume nutrients and produce electrons, protons, and CO_2. After being transported through the external circuit, the electrons react with protons and O_2 on the cathode, carrying out the oxidation-reduction reaction (ORR) to generate water.[5]

Anodes serve as the bacterial habitat and greatly impact the performance of MFCs. Researchers attempted to enhance the performances of MFCs by modifying the anode materials (Table S1, Supporting Information).[6–23] Porous carbon is viewed as a good anode material because of its high surface area for bacterial attachment, better conductivity for electron transfer, and easier to be functionalized.[4,24,25] On the other hand, the cathode ORR catalyst[26] is also a detrimental factor that limits the power output of the MFC.[27,28] Platinum-based materials are commonly used as the cathode catalysts in MFCs; however, the high cost and low cycle stability need to be addressed.[29,30] Cost-effective materials with high activity and conductivity, as listed in Table S2, , Supporting Information, are alternatives

C.-C. Hsu, Y.-C. Lin, Y.-Y. Lin, H.-T. Li, C.-S. Ni, C.-I. Liu, S.-F. Liu, H.-Y. Chen
Department of Material Science and Engineering
National Tsing Hua University
101, Sec. 2, Kuang-Fu Road, Hsinchu 30013, Taiwan
E-mail: hanyi.chen@mx.nthu.edu.tw

The ORCID identification number(s) for the author(s) of this article can be found under https://doi.org/10.1002/aesr.202100163.

© 2021 The Authors. Advanced Energy and Sustainability Research published by Wiley-VCH GmbH. This is an open access article under the terms of the Creative Commons Attribution License, which permits use, distribution and reproduction in any medium, provided the original work is properly cited.

DOI: 10.1002/aesr.202100163

C.-C. Chang
Graduate Institute of Environmental Engineering
National Taiwan University
No. 1, Sec. 4, Roosevelt Road, Taipei 106, Taiwan

T.-Y. Liu
Institute of Bioinformatics and Structural Biology & Department of Life Science
National Tsing Hua University
101, Sec. 2, Kuang-Fu Road, Hsinchu 30013, Taiwan
E-mail: tzliu@life.nthu.edu.tw

L.-C. Lin, Y.-T. Pan
Department of Chemical Engineering
National Tsing Hua University
101, Sec. 2, Kuang-Fu Road, Hsinchu 30013, Taiwan

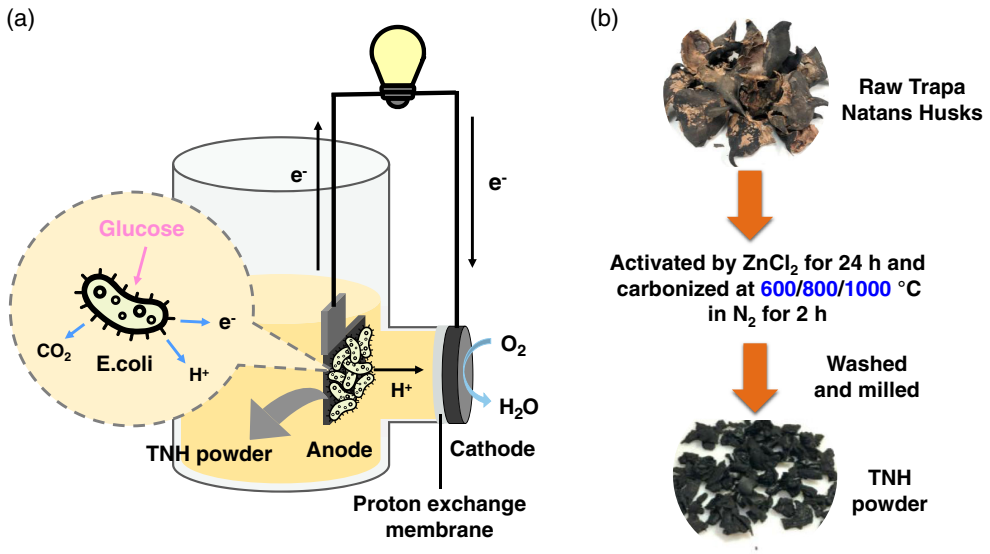


Figure 1. a) MFC construction and b) synthesis process of *Trapa natans* husk-derived nanoporous carbon (TNH).

to platinum-based cathodes.[27,31–43] It is worth noting that there are different methods to measure the power densities of MFCs. Some researchers have addressed the differences between the linear sweep voltammetry (LSV) method and the method of varying the output load constant resistance (CR).[44,45] The power densities measured by LSV with 1 mV s^{-1} scan rate were about two times larger than those of CR. To compare our results with those from other references, we tested both the LSV and CR methods in this study. And the results are also listed in Table S1 and S2, Supporting Information.

Desirable properties for anode and cathode are similar. High surface area is important for bacterial attachment to the anode and oxygen adsorption on the cathode. A remarkable conductivity contributes to a better electron transfer efficiency on both the anode and cathode. The functional groups also play a crucial role in the hydrophilicity of the anode and serve as active sites that facilitate the ORR on the cathode. Therefore, in this study, we attempted to produce an activated carbon-based material that can be simultaneously applied to both the anode and cathode.

Over 1300 tons of *T. natans* husks are produced in Taiwan every year As a result, utilizing the agricultural waste-derived nanoporous carbon electrodes not only lowers the cost of MFCs but also reduces the air pollution produced from agricultural combustion. In this study, the nanoporous carbon was successfully derived from *T. natans* husks with a $ZnCl_2$ activation agent at different carbonization temperatures (600, 800, and 1000 °C). The *Escherichia coli* system-based MFCs exhibited a significantly enhanced electrochemical performance after substituting the CAC materials on the anode and cathode with TNH. We showed that the MFCs without platinum-based electrodes still achieve a high average power density of 5713 mW m^{-2}, demonstrating that TNH is a promising low-cost electrode material for MFCs, and warrants further study.

The reaction activities of the ORR on MFC cathode materials are commonly investigated via rotating disk electrodes (RDEs) or rotating ring disk electrodes.[34,46–49] However, how the microscale properties of cathode materials affect the electrochemical reactions and activities of the catalyst is not fully understood. Scanning electrochemical microscopy (SECM) is a powerful technique for studying microscale interfacial electrochemical reactions, including metal ion batteries,[50–54] biochemical,[55–57] corrosion,[58] and catalyst behaviors.[30,59–63] By scanning the interface with a microelectrode at a close distance, the local electrochemical reaction activity can be obtained as a current collected by the microelectrode owing to the variations in the local reaction rates.[64–66] In this study, SECM experiments were performed with a four-electrode setup. Two platinum wire electrodes were used as the counter and reference electrodes. A 10 μm microelectrode probe with a fused silica insulating sheath was used as the working electrode, and a catalyst-coated platinum plate was used as another working electrode. The activities of ORR catalyst were measured in this study by using the tip generation/substrate collection (TG/SC) mode. Figure S1, Supporting Information, shows the principle of the SECM measurement.

Supercapacitors (SCs) are highly efficient energy storage devices that function in transient energy delivery and energy recovery.[67,68] To harvest the electrical energy generated from the MFCs, we used SCs with TNH electrodes as auxiliary power sources in this study. Our TNH-based SC exhibited a high capacitance of 84 F g^{-1} at a current density of 1 A g^{-1}, revealing a sustainable energy storage characteristic. Furthermore, we placed a DC–DC power boost converter between SCs and LED to increase the output power (P_{out}) of the SCs able to power the LEDs. This TNH-based MFC-SC system allows successful incorporation of the energy storage devices into cost-effective MFCs for sustainable energy generation.

2. Results and Discussion

2.1. Material Characterization of TNHs

The nanoporous TNHs were prepared with a $ZnCl_2$ activator at different carbonization temperatures ($T = 600$, 800, and 1000 °C;

© 2021 The Authors. Advanced Energy and Sustainability Research published by Wiley-VCH GmbH

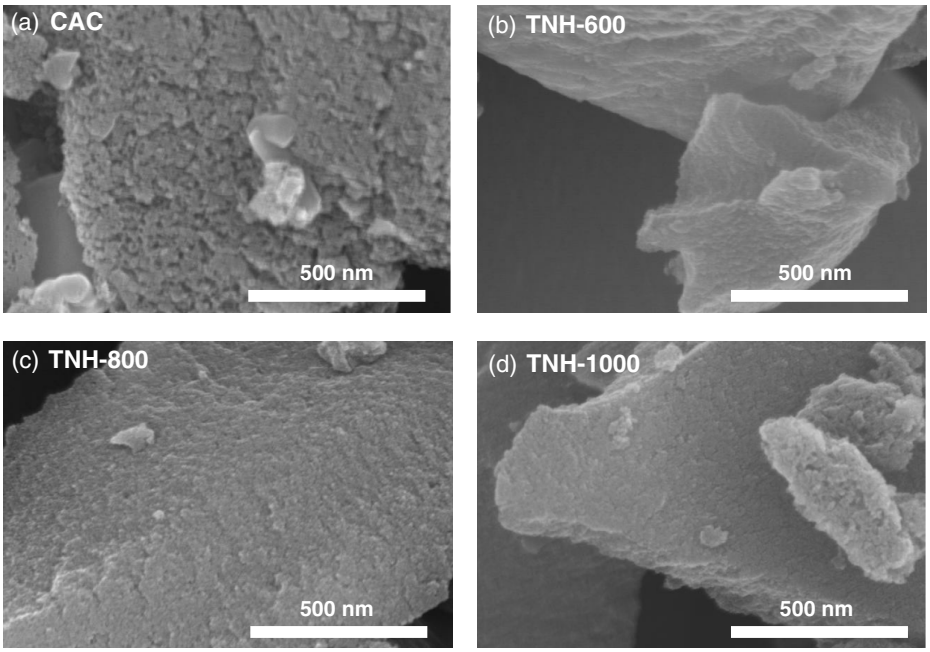


Figure 2. SEM images of TNH and CAC. a) CAC, b) TNH-600, c) TNH-800, and d) TNH-1000.

labeled as TNH-600, TNH-800, and TNH-1000, respectively). The scanning electron microscopy (SEM) images in **Figure 2** show that the surface morphologies of the CAC and TNHs were rough. The SEM images of untreated raw TNH (rTNH) and TNH-600 without the activation process (rTNH-600) are shown in Figure S2, Supporting Information. Compared with the smooth surface of rTNH and rTNH-600, TNHs were successfully activated by $ZnCl_2$. The Brunauer–Emmett–Teller (BET) results (**Figure 3**a) reveal that all the TNHs have higher specific surface areas (TNH-600: 1499.2 $m^2 g^{-1}$; TNH-800: 1323.6 $m^2 g^{-1}$; and TNH-1000: 1374.6 $m^2 g^{-1}$) than the CAC (832.1 $m^2 g^{-1}$). IUPAC-defined pores can be classified into three classes, namely, macropores (>50 nm), mesopores (2–50 nm), and micropores (<2 nm).[69] These samples exhibited hysteresis loops classified as the H4-type (IUPAC classification), implying that the major pores are micropores and mesopores. These results are also consistent with the BET results (Figure 3b–d). The BET analyses of rTNH and rTNH-600 are also shown in Figure S3, Supporting Information. The specific surface areas and the pore volume of both the rTNH and rTNH-600 are much smaller than that of the CAC and the TNHs with the activation processes. Analyses of the BET surface areas and pore parameters of the samples showed that the TNHs exhibited almost twice the surface area of the CAC, which is due to the high content of micropores and mesopores (**Table 1**). Furthermore, when the carbonization temperature increased from 600 to 1000 °C, the micropores decreased, and the mesopores and macropores increased. This indicates that the higher temperature assisted the activation process, and thus, the pore size increased. The mesoporous structure acts as a highway to facilitate the reactions at the catalytic sites, thus improving the ORR performance.[70]

All the samples in Figure 3e show similar XRD patterns with the (002) and (100) characteristic peaks of activated carbon.[71] The broad peaks are not obvious, which indicates that the TNHs are amorphous carbon because of their porous structure. CAC was not acid treated, so it still contained impurities (labeled as *). Figure 3f shows the related Raman spectra. The D-band and G-band intensity ratios (I_D/I_G) were calculated by Lorentz curve fitting. The D-band in the Raman spectra refers to a disordered graphitic lattice structure with sp^3, while the G-band is recognized as the vibrations of the sp^2 bonds in carbon.[72] The I_D/I_G ratio represents the degree of carbonization of TNHs. A higher I_D/I_G value indicates more defects in the carbon material. The calculated I_D/I_G ratios of the TNHs were all smaller than that of the CAC, which corresponds to the better carbonization structure.

The surface chemical properties, including composition, bonding characteristics, and chemical state, are vital factors associated with bacterial attachment on the anodes and catalyst active sites of the cathode. X-ray photoelectron spectroscopy (XPS) was used to detect these properties. The C 1*s* and N 1*s* peaks in **Figure 4** can be regarded as a combination of several peaks. The dominant peaks of C 1*s* at 284.4 ± 0.1 eV and 285 ± 0.1 eV are due to the high amount of the graphitic structure (C═C) and hybridized carbon (C—C), respectively. The smaller peaks at 286 ± 0.2, 286.9 ± 0.2, and 289.0 ± 0.2 eV were attributed to the phenolic (C—O), carbonyl (C═O), and carboxyl groups (O—C═O), respectively.[73] **Table 2** lists the percentages of elements and bonds. The nitrogen content of TNH shows that our process was successfully doped with nitrogen. When the anode properties and a higher percentage of O-functional groups are considered, the nanoporous carbons exhibited a larger polarity as formed by the bonds. However, as the carbonization temperature increased, the number of O-functional groups gradually decreased. The TNH-600 and TNH-800 contained higher percentages of O-functional groups than the TNH-1000 and CAC,

© 2021 The Authors. Advanced Energy and Sustainability Research published by Wiley-VCH GmbH

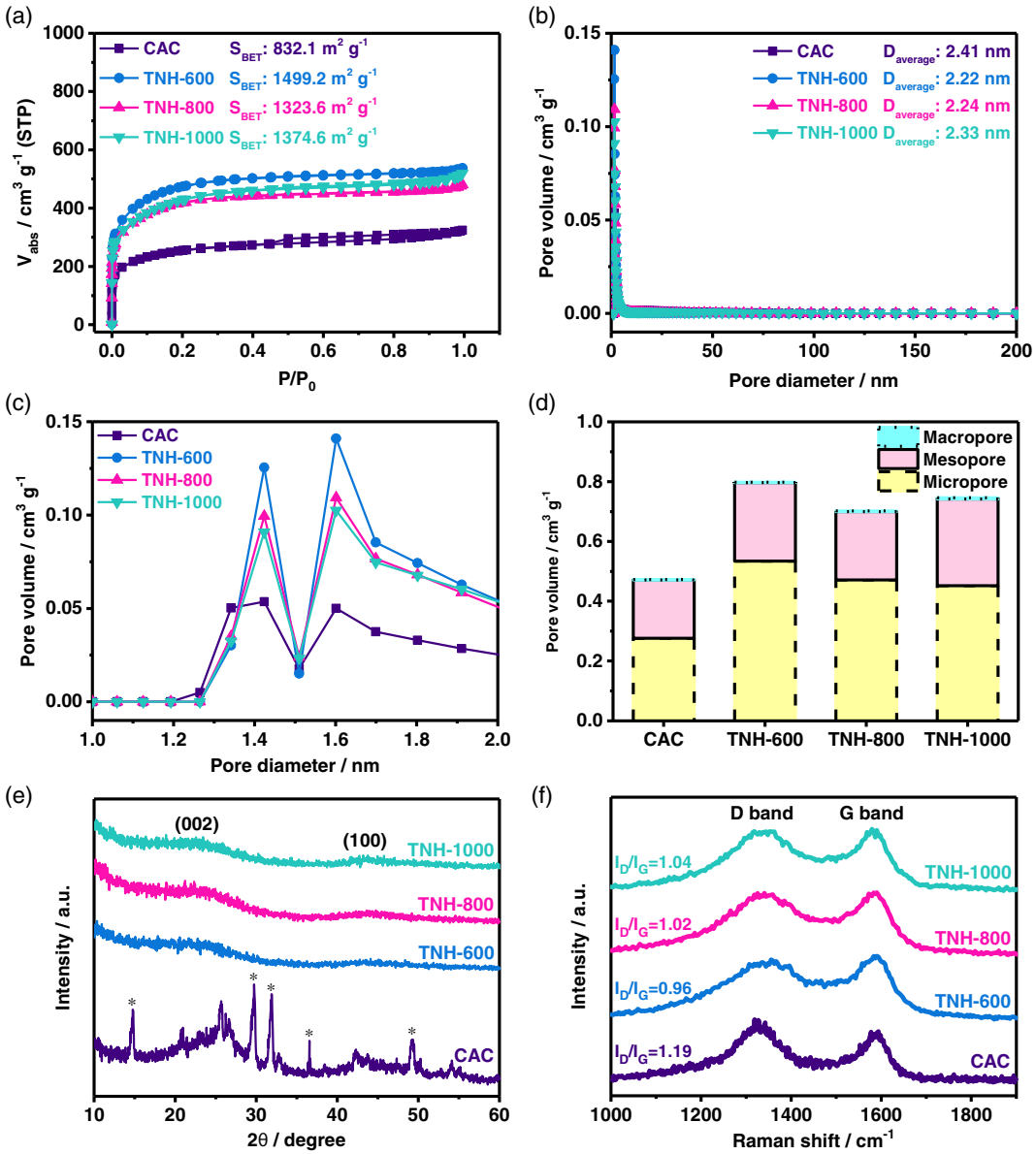


Figure 3. a) BET curves, b) BJH pore size distribution plots, c) magnified BJH pore size distribution plots, and (d) pore size distribution bar graph of CAC, TNH-600, TNH-800, and TNH-1000. S_{BET} is the specific surface area and $D_{average}$ is the pore diameter. e) X-ray diffraction (XRD) patterns and f) Raman spectra of CAC, TNH-600, TNH-800, and TNH-1000 (*: impurities).

Table 1. BET surface area and pore parameters of TNH and CAC.

	S_{BET} [$m^2 g^{-1}$][a)]	$D_{average\ pore}$ [nm]	V_{micro} [$cm^3 g^{-1}$]	V_{meso} [$cm^3 g^{-1}$]	V_{macro} [$cm^3 g^{-1}$]	V_{total} [$cm^3 g^{-1}$]
rTNH	1.2	19.31	0	0.002 (40.0%)	0.003 (60.0%)	0.005
rTNH-600	19.8	5.46	0.006 (26.1%)	0.009 (39.1%)	0.008 (34.8%)	0.023
CAC	832.1	2.41	0.276 (58.3%)	0.195 (41.2%)	0.002 (0.5%)	0.473
TNH-600	1499.2	2.22	0.534 (66.9%)	0.263 (33.0%)	0.001 (0.1%)	0.798
TNH-800	1323.6	2.24	0.471 (67.2%)	0.229 (32.6%)	0.002 (0.2%)	0.702
TNH-1000	1374.6	2.33	0.452 (60.2%)	0.29 (38.9%)	0.004 (0.5%)	0.746

[a)] V_{macro}, macropore volume; V_{micro}, micropore volume; V_{meso}, mesopore volume; and V_{total}, total pore volume.

© 2021 The Authors. Advanced Energy and Sustainability Research published by Wiley-VCH GmbH

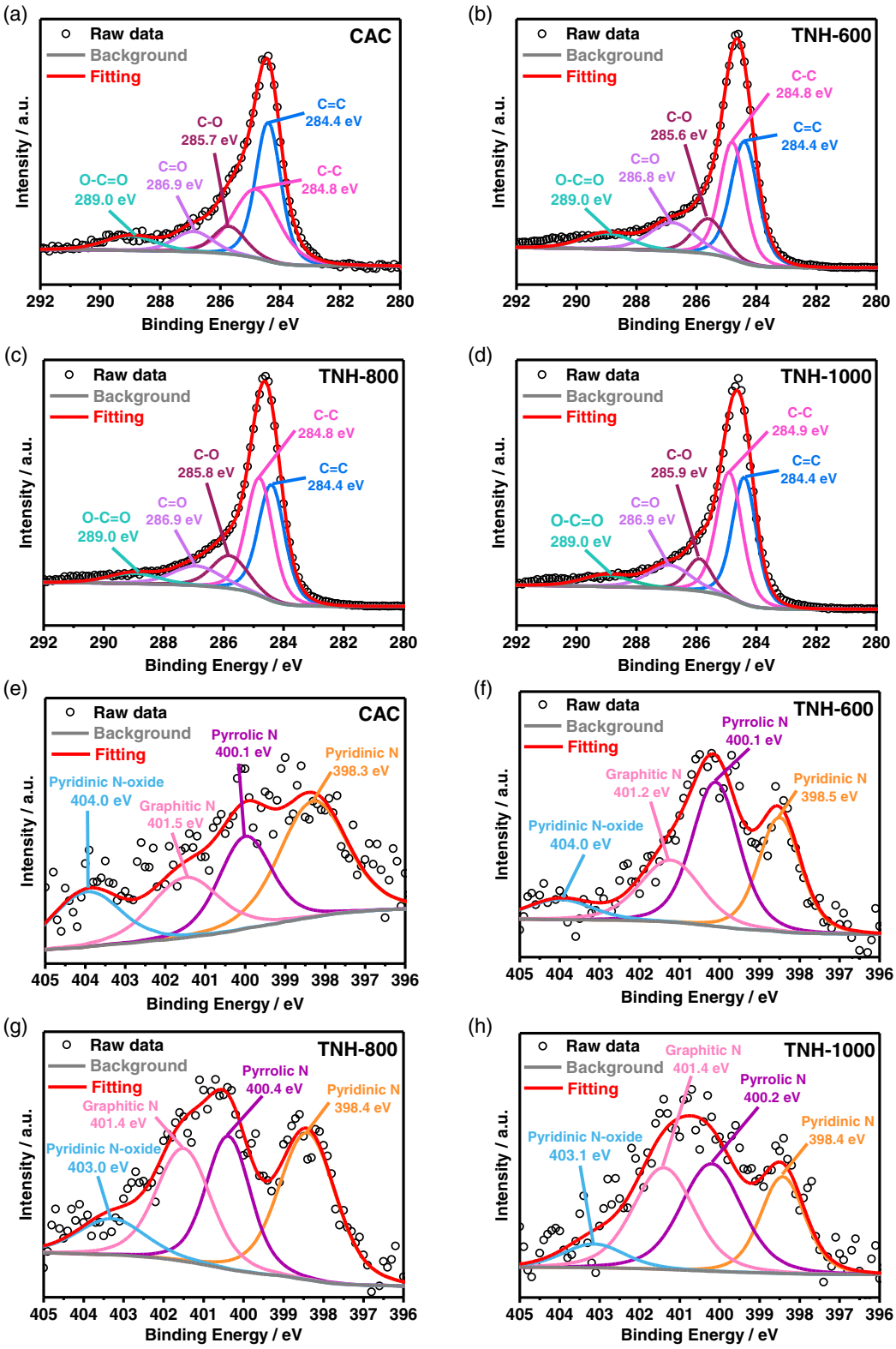


Figure 4. XPS C 1s profiles of a) CAC, b) TNH-600, c) TNH-800, and d) TNH-1000. N 1s profiles of e) CAC, f) TNH-600, g) TNH-800, and h) TNH-1000.

which means that the two samples exhibited a more significant polarity among all the nanoporous carbons. Furthermore, it was noted that the nanoporous carbon with nitrogen can enhance hydrophilicity and biocompatibility.[74] The different chemical

© 2021 The Authors. Advanced Energy and Sustainability Research published by Wiley-VCH GmbH

Table 2. Surface components of TNHs and CAC.

Elements and functional groups		CAC	TNH-600	TNH-800	TNH-1000
Element (%)	C	76.49	92.45	91.38	92.53
	N	1.13	1.29	1.86	1.27
	O	22.37	6.26	6.76	6.20
C-containing groups (%)	sp^2	46.85	25.21	38.63	39.17
	sp^3 carbon/C—N	27.77	38.65	29.39	34.81
	C—O	9.85	16.98	12.01	7.98
	C=O	8.61	11.43	12.56	12.08
	O—C=O	6.92	7.73	7.42	5.95
N-containing groups (%)	Pyridinic N	38.31	29.26	37.94	23.12
	Pyrrolic N	23.62	40.22	24.87	35.48
	Graphitic N	19.90	22.64	26.79	35.56
	Pyridinic N-oxide	18.17	7.88	10.40	7.85

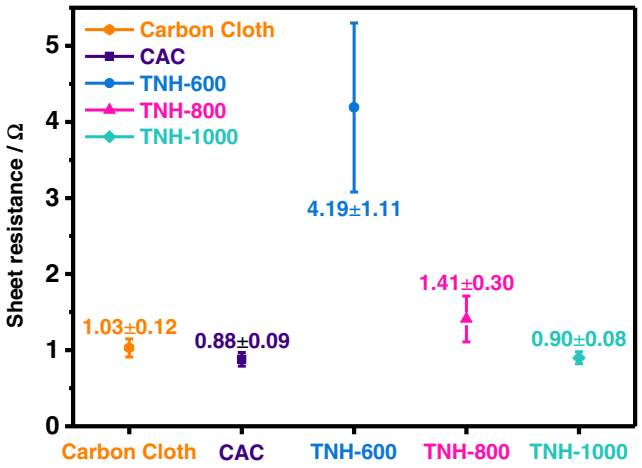


Figure 5. Sheet resistance of carbon cloth, CAC, TNH-600, TNH-800, and TNH-1000 ($n = 7$).

states of the N-functional group play different roles in the ORR on the cathode. For further investigation of the active sites in the ORR reaction, the different nitrogen groups, namely, pyridinic-N, pyrrolic-N, graphitic-N, and pyridinic-N-oxide, were deconvoluted into four peaks at 398.3–398.7 eV, 400.1–400.5 eV, 401.2–401.4 eV, and 402–404 eV, respectively. The pyridinic-N and pyrrolic-N percentages declined at higher carbonization temperatures, while the graphitic-N percentage increased. Because of the increase in carbonization temperatures, the thermally unstable pyridinic-N and pyrrolic-N were transformed to the graphitic-N. This phenomenon has been reported by previous studies.[27,75,76] Their results indicated that pyridinic-N was the active site for facilitating the ORR by conducting electron transfer;[40] however, the enrichment of graphitic-N was more crucial to the ORR activity, and the graphitic-N also favored oxygen adsorption.[77] Our results showed that the TNH-1000 possessed the highest percentage of graphitic N, indicating its high ORR catalytic ability.

Figure S4, Supporting Information, shows the static contact angles (SCAs) of water droplets on the TNHs. The SCA is related to the hydrophilicity of activated carbons and mainly affected by the number of O-functional groups. The SCAs of CAC, TNH-600, TNH-800, and TNH-1000 were 117.9°, 99.5°, 84.2°, and 103.6°, respectively. A higher SCA indicates a lower hydrophilicity of the carbon materials. TNHs have a lower SCA than CAC, which can be attributed to their large polarity and high amounts of N- and O-containing functional groups. These results also revealed that TNH-1000 exhibited poor hydrophilicity because the carbonization process removed most of the functional groups.

Figure 5 shows that the sheet resistance of the carbon cloth, CAC, TNH-600, TNH-800, and TNH-1000 was 1.03, 0.88, 4.19, 1.41, and 0.90 Ω, respectively. Compared with the XPS results, the C=C content increased when the carbonization temperature increased, leading to better conductivity. This shows that TNH-1000 exhibited the lowest resistance and the poorest hydrophilicity. Moreover, the sheet resistance of TNH-800 was significantly lower than that of TNH-600. The higher sheet resistance of TNH-600 was attributed to a higher number of O-functional groups, despite the higher hydrophilicity.

2.2. Electrochemical Characterization

The LSV curves of CAC and TNHs in **Figure 6** were measured using RDEs. A higher half-wave potential (E_{half}) and a larger

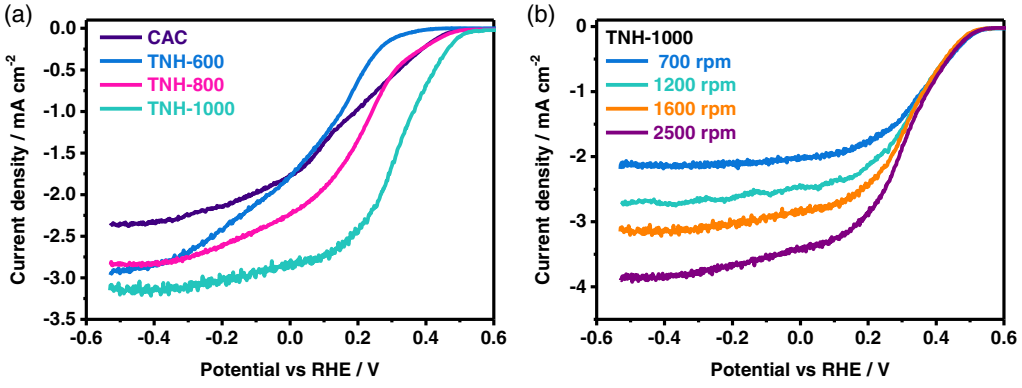


Figure 6. LSV curves of a) CAC, TNH-600, TNH-800, and TNH-1000 at 1600 rpm, and b) TNH-1000 with different rotation speeds.

© 2021 The Authors. Advanced Energy and Sustainability Research published by Wiley-VCH GmbH

limited current indicate a better catalyst activity. Concerning the material analysis, TNH-1000 presented a high specific surface area, which provides a larger reaction area and larger amounts of graphitic-N and pyridinic-N to increase the ORR activity. Furthermore, it also exhibited the lowest sheet resistance as compared to other TNHs. Therefore, TNH-1000 exhibited the best ORR catalyst activity among all the nanoporous carbons.

SECM measurements were conducted to further investigate the ORR catalyst activity sites of the different activated carbons. The cyclic voltammetry (CV) curves of the probe and substrate are shown in Figure S5, Supporting Information. According to the CV curve results, the probe and substrate potentials were set to −0.4 and −0.02 V (vs Pt), respectively, and formed the TG/SC mode. The distance between the probe and substrate was maintained at approximately 40 µm by performing an approaching curve test, as shown in Figure S5c, Supporting Information. SECM was conducted in the TG/SC mode. Four different catalysts were coated on four regions of the platinum plate substrate so that four catalysts could be measured under almost the same conditions. This would allow the results to be compared. The said results are shown in **Figure 7**, where a warmer color indicates a higher current. TNH-1000 activated carbon contributed a higher current than the other three catalysts, showing the highest electrochemical catalyst activity among the four activated carbons.[30] This result is expected because TNH-1000 provides the highest percentage of graphitic-N as determined by XPS, the most excellent conductivity from the sheet resistance, and the highest amount of mesopores, all of which facilitate the ORR. Moreover, in combination with the RDE results, TNH-1000 exhibited the highest electrochemical capability.

2.3. Electrochemical Performances of TNH Anodes in MFCs

The electrochemical activities of the TNH electrodes in MFC before and after inoculation with *E. coli* were investigated with CV (Figure S6, Supporting Information). The short-dashed line shows the CV curves before inoculation with *E. coli*, while the solid line represents the CV curves after 16 h of inoculation. The CV curves before inoculation display a rectangular shape, which represents the double-layer capacitive properties of the carbon materials.[78] After 16 h of microbial growth, the oxidation current increased significantly, indicating that biofilm was successfully formed on the anode as electrons were transferred more efficiently from the bacteria to the anode through the biofilm. After inoculation, the large oxidation current of TNH-800 resulted in an excellent electron transfer efficiency and electrochemical activity, possibly aided by the functional groups, the low resistivity, and the high bacterial attachment.

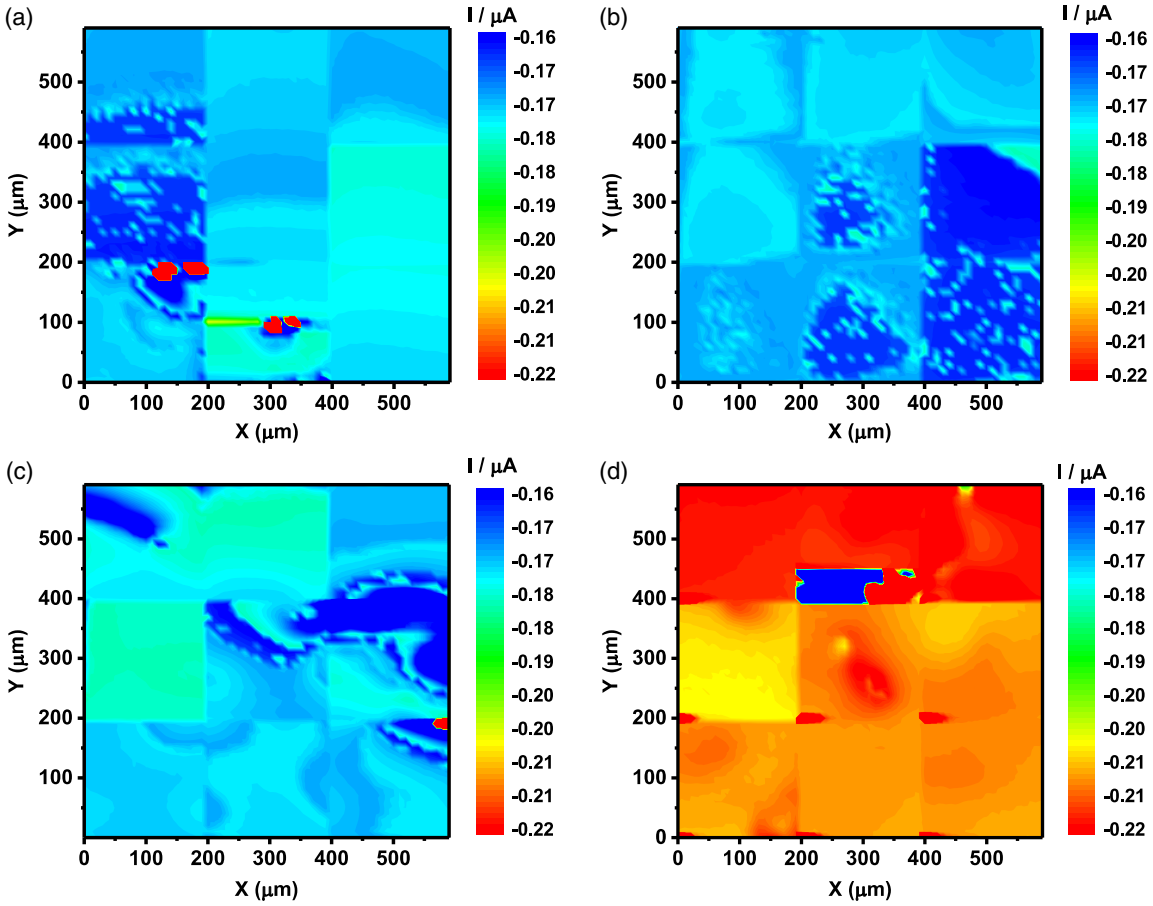


Figure 7. SECM probe current results of a) CAC, b) TNH-600, c) TNH-800, and d) TNH-1000. The distance between the probe and the catalysts was ≈40 µm.

© 2021 The Authors. Advanced Energy and Sustainability Research published by Wiley-VCH GmbH

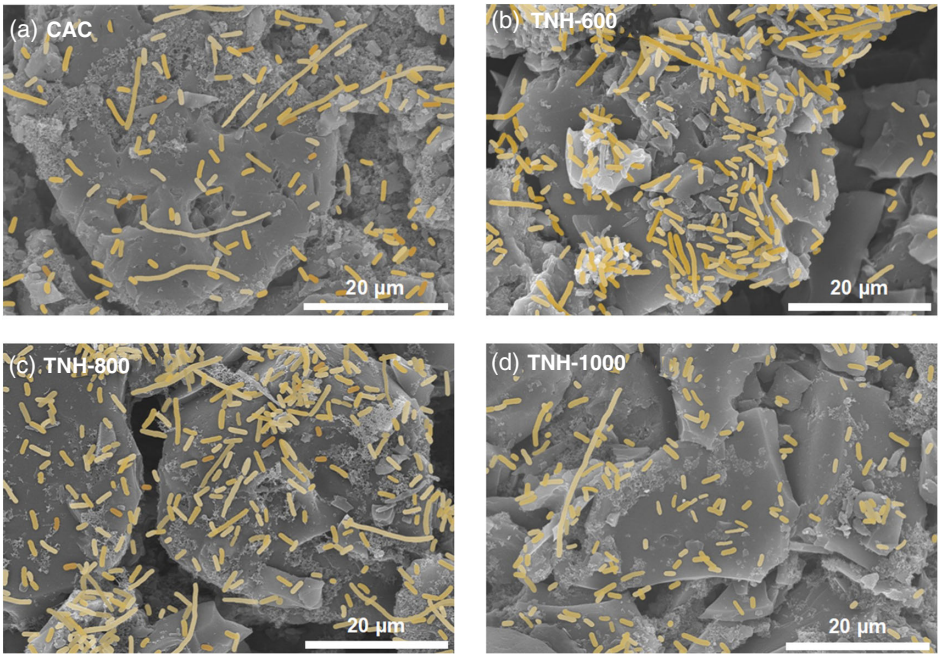


Figure 8. SEM images of the *E. coli* adhesion on a) CAC, b) TNH-600, c) TNH-800, and d) TNH-1000.

Figure 8 shows SEM images of the *E. coli* adhesion to the anode. The yellow rod-shaped microbes indicate the distribution of *E. coli*. The microbes were abundantly attached to the surface of the TNH-600 and TNH-800 anodes because of their favorable hydrophilicity and porous structure. The poorer attachment of microbes to CAC may result from the relatively low surface area and the low N-functional group. The poor microbe attachment on TNH-1000 may be due to its high degree of carbonization and the poor hydrophilicity.

2.4. MFC Performance with Various TNH Anodes

Single-chamber MFCs, with CAC as the cathode and CAC, TNH-600, TNH-800, or TNH-1000 as the anode, were fabricated to optimize the anode materials. The power density data and polarization curves for the MFCs were obtained by LSV at a scan rate of 1 mV s^{-1} from the open-circuit voltage (OCV) to 0 mV. The average power densities of the MFCs with CAC, TNH-600, TNH-800, and TNH-1000 anodes were 2998, 3851, 5115, and 4017 mW m^{-2}, respectively (**Figure 9**). The MFC with the TNH-800 anode exhibited the highest average power density of all the modified anodes. Furthermore, these results support the notion that activated carbons with high porosity are favorable for bacterial adhesion, as concluded by Ilomuanya et al.[79]

TNHs have a highly porous structure, which enables a higher surface area. Furthermore, the four-point probe measurements showed that TNH-800 and TNH-1000 were carbonized to a higher graphitic level and had a significantly lower resistivity than TNH-600. However, TNH-800 exhibited better hydrophilicity and a higher number of O-functional group than TNH-1000,

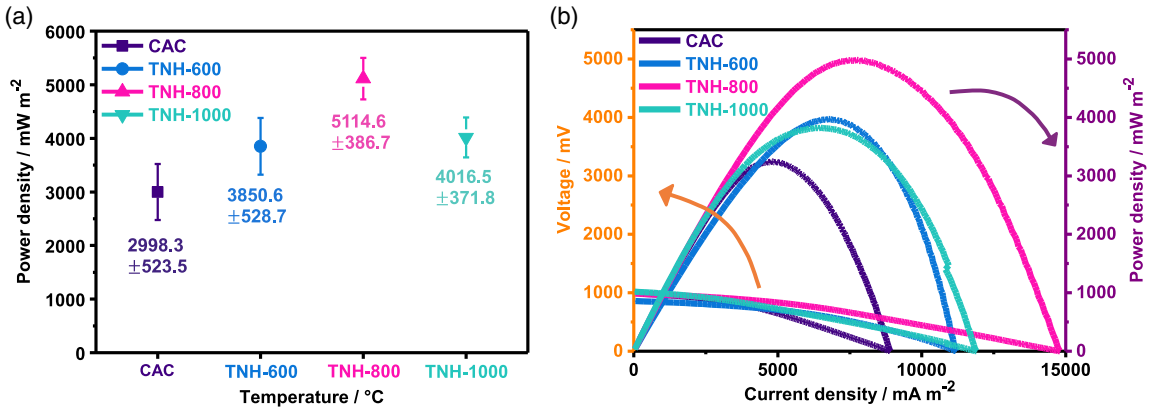


Figure 9. MFC performance with a CAC cathode and various anodes. a) Power densities of the different modified anodes ($n = 3$) and b) polarization and power density curves of the different modified anodes in the MFCs.

© 2021 The Authors. Advanced Energy and Sustainability Research published by Wiley-VCH GmbH

which possessed a higher biocompatibility and thus the highest power density in the MFCs.

2.5. Performance of MFCs with Various TNH Cathodes

For further investigation of the performance of the different cathode materials, the optimized sample, TNH-800, was fixed as the anode material and the cathode material was changed from CAC to the different TNHs. The MFC with the TNH-1000 cathode exhibited a maximum average power density of 5713 mW m^{-2} (**Figure 10**a,b). The average power densities for the MFCs with CAC, TNH-600, TNH-800, and TNH-1000 cathodes were 5115, 4340, 5138, and 5713 mW m^{-2}, respectively. Additionally, the anode potentials in the three-electrode polarization curve (Figure 10c) were similar during discharging in all MFCs, indicating that the varying cathodes contributed to the different performances.

Although the specific surface area of the TNHs was prominently larger than CAC, the cathode performance of the TNHs was not significantly better. However, it corresponded to the sheet resistance and N functional group analyses that the lower resistance and higher amount of N functional group help to increase the power output. As a result, we concluded that the conductivity and the concentration of the graphitic-N are vital factors for the performance of MFC cathode, which supports the notion of TNH-1000 being the best ORR catalyst for MFCs.

Because there are different ways of measuring the power density applied for MFCs and the outcomes are prominently distinct, the polarization curves and the power densities were measured both by LSV and CR. The maximum power densities of the cathode//anode (i.e., CAC//CAC, CAC//TNH-800, and TNH-1000//TNH-800) obtained by LSV were 3247, 4970, and 5661 mW m^{-2}, respectively, as shown in **Figure 11**a. On the other hand, the power densities of CAC//CAC, CAC//TNH-800, and TNH-1000//TNH-800 measured by CR were 1458, 2169, and 2549 mW m^{-2}, respectively (Figure 11b). The CR results were ≈2.28-fold smaller than the result obtained by LSV. The prominent differences were attributed to the small anodic and cathodic areas, which resulted in the large ohmic resistance of our MFCs. The maximum power densities of TNH-1000//TNH-800 obtained from both the LSV and CR methods are higher than those from most of the MFCs listed in Table S1 and Table S2, Supporting Information. These results

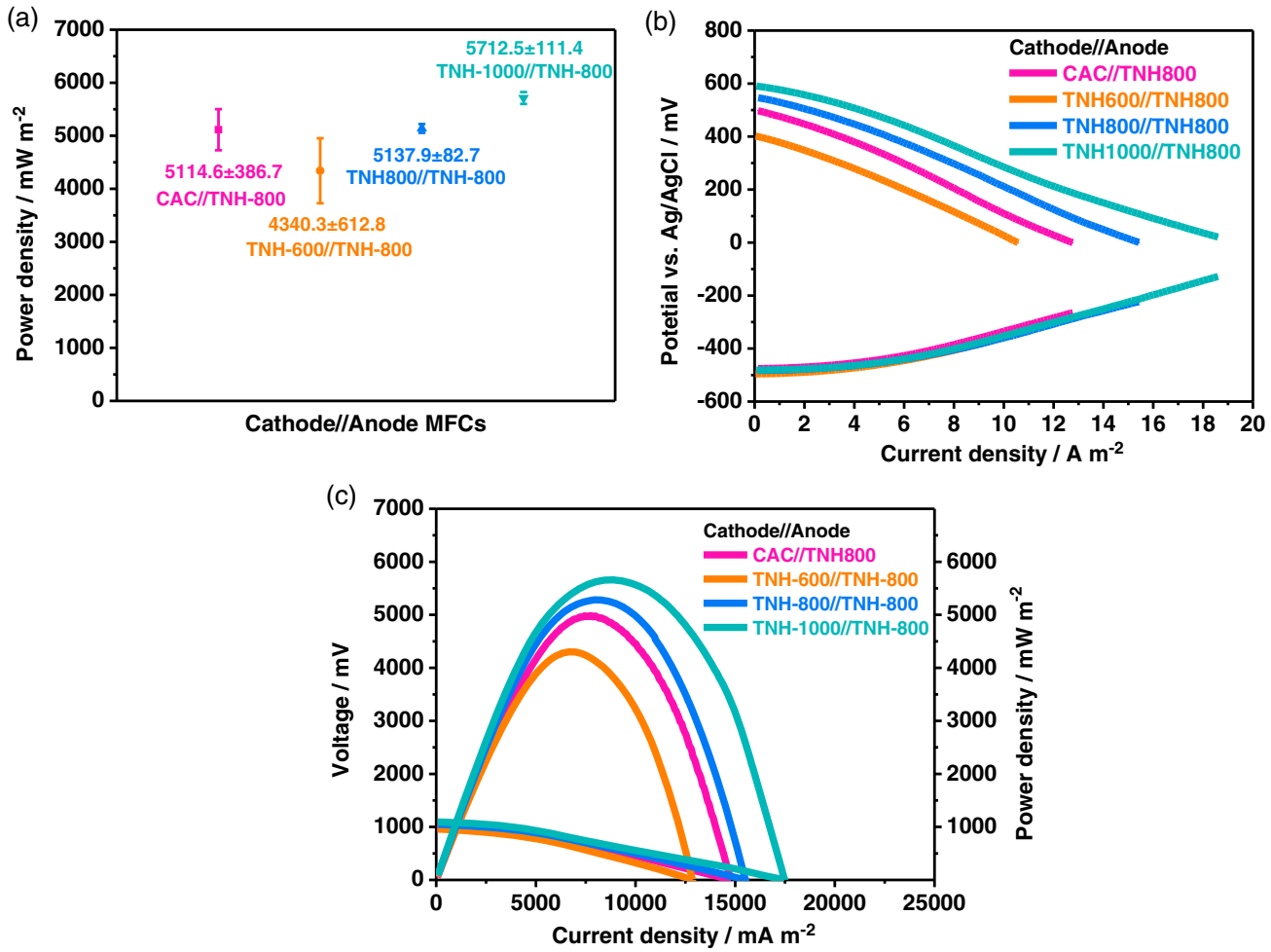


Figure 10. MFC performance with TNH-800 as the anode and various cathodes. a) Power densities of the different modified cathodes ($n = 3$), b) polarization and power density curves of the different modified cathodes in the MFCs, and c) three-electrode polarization curves.

© 2021 The Authors. Advanced Energy and Sustainability Research published by Wiley-VCH GmbH

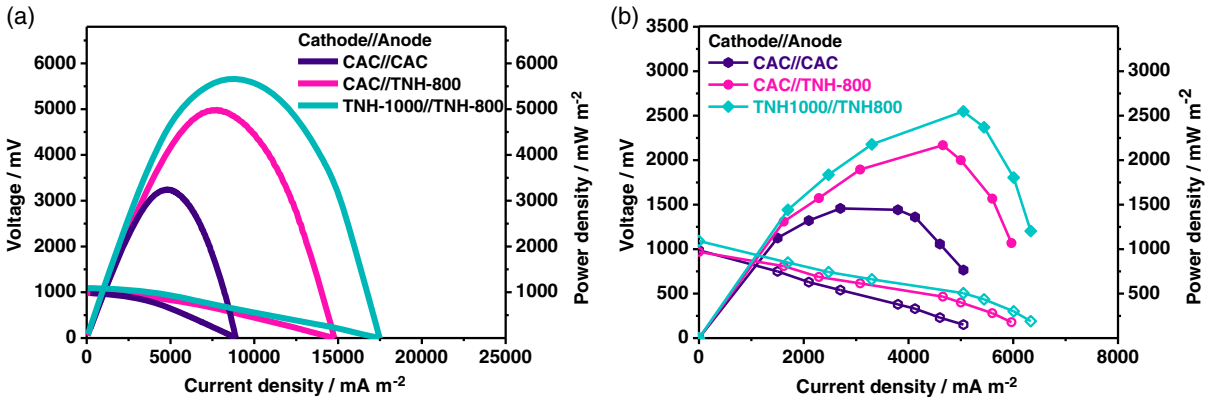


Figure 11. Comparison of the polarization and power density curves measured by a) LSV at 1 mV s^{-1} and by b) CR.

demonstrate that the biowaste-derived TNHs exhibited outstanding power generation in MFC systems and can be used as a promising electrode material for future studies. Moreover, the reuse of *T. natans* husks reduces the cost of devices and aligns with the circular economy for green energy production.

Furthermore, the long-term stability of the MFCs was also evaluated. The MFC devices were operated for 150 h followed by 4 h rests without nutrition refreshment. As shown in **Figure 12**a, the maximum OCV of (1000-800) and (CAC-CAC) reached 1060 and 900 mV, and stabilized at around 700 and

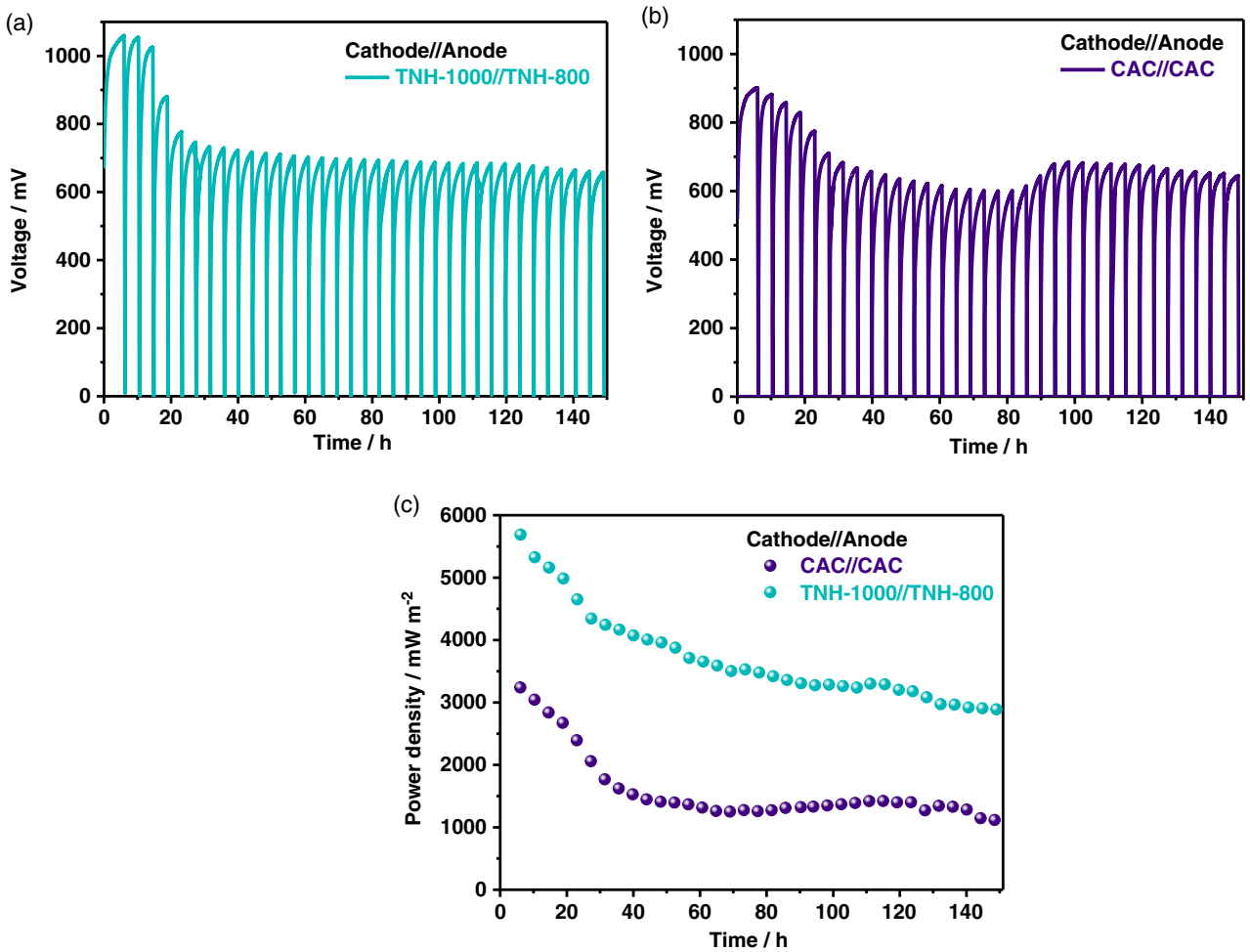


Figure 12. Long-term stability of cell voltage of a) CAC//CAC MFC, b) TNH-1000//TNH-800 MFC, and c) power output of CAC//CAC and TNH-1000//TNH-800 MFCs.

© 2021 The Authors. Advanced Energy and Sustainability Research published by Wiley-VCH GmbH

600 mV, respectively. The dividing point was at running for 20–30 h, where the decreasing OCV approached to a steady state. It is because that the electrolyte could not supply sufficient nutrition to achieve the maximum OCV. The observation was similar in the tendency of the power density curves (Figure 12b), which turned to decrease at a much slower rate. The stable phase was due to bacteria self-feeding with the dead ones and reached dynamic equilibrium in their chain of survival.[8,11] The outperformance of the MFCs of TNHs as both electrode materials still exhibited in the long-term phase, which represents that the TNHs are confidently a prospective electrode material for MFCs self-rechargeable system.

2.6. Performance of SCs with TNH Electrodes

This study also employed TNH as electrodes in symmetric SCs to store the electricity generated by TNH-based MFCs. **Figure 13**a illustrates the galvanostatic charge/discharge (GCD) curves of various nanoporous carbon-based SCs at a current density of 1 A g^{-1}. The capacitances of the symmetric SCs with the CAC, TNH-600, TNH-800, and TNH-1000 electrodes were 34, 84, 82 and 65 F g^{-1}, respectively. All the TNH-based SCs exhibited higher capacitances than the CAC-based SC, which is due to the TNHs having higher surface areas than the CAC. The long-term cycle stability test under a current density of 1 A g^{-1} is shown in Figure 13b. Both TNH-600 and TNH-800 exhibited specific capacitances exceeding 80 F g^{-1} which sustained for 1000 cycles without fading, demonstrating their excellent cycling stabilities.

Figure 13c depicts the CV curves of the examined electrodes at a scan rate of 10 mV s^{-1} and in the voltage range of 0 to 1.6 V. All the SCs exhibited an almost rectangular shape, showing double-layer capacitance characteristics. The specific capacitances shown in Figure 13d were calculated based on the CV curves. Although no obvious distinction was observed between TNH-600 and TNH-800 at the low scan rate of 2 mV s^{-1}, TNH-600 stood out and achieved almost 30 F g^{-1} at a high scan rate of 100 mV s^{-1}, which is nearly threefold higher than the others. This indicates that the SCs with TNH-600 electrodes could provide high capacitance at both low and high rates. Furthermore, the specific capacitance trends were as follows: TNH-600 > TNH-800 > TNH-1000 > CAC. The capacitance decreased with an increasing carbonization temperature, which can be attributed to the presence of oxygen-containing functional groups.

The SC with the TNH-600 electrode exhibited the best performance among all the nanoporous carbon-based SCs. This may result from its high surface area and oxygen-containing functional groups, which improves the surface hydrophilicity of nanoporous carbon, and hence increases the specific capacitance. As the most optimized SC electrode, TNH-600 was used to assemble SCs to store the electricity of the TNH-based MFCs.

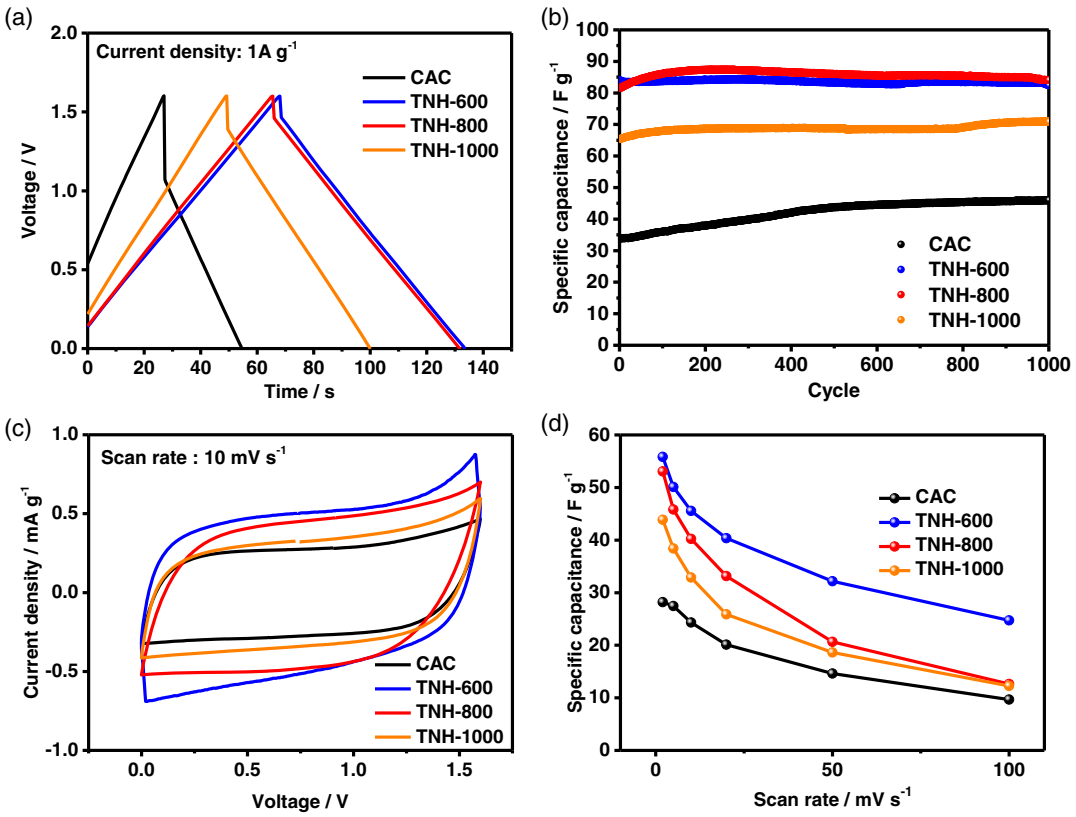


Figure 13. Electrochemical performances of the TNH-600, TNH-800, TNH-1000, and CAC electrodes in 1 M Na_2SO_4 in a two-electrode configuration. a) GCD curves at a current density of 1 A g^{-1}, b) long-term cycling stability at a current density of 1 A g^{-1}, c) cyclic voltammograms at a scan rate of 10 mV s^{-1}, and d) specific capacitances at various scan rates (2, 5, 10, 20, 50, and 100 mV s^{-1}).

© 2021 The Authors. Advanced Energy and Sustainability Research published by Wiley-VCH GmbH

2.7. TNH-Based MFC-SC System with DC–DC Converter

A circuit system was designed to store the electricity generated by the TNH-based MFCs (TNH-1000//TNH-800) to the TNH-based SCs (TNH-600), which was used to power LEDs. The MFCs offered a robust power source for the circuit system, allowing a blue LED to function properly, as shown in **Figure 14**. The equation for the conversion efficiency is shown in Equation (1). The experimental conversion efficiency (η) of the circuit system was approximately 60%. The P_{out} was measured at the output pin of the converter IC, and the input current (I_{in}) and voltage (V_{in}) were measured during the operation of MFC.

$$\eta = P_{out}/(V_{in}I_{in}) \quad (1)$$

MFCs and supercapacitors were used as the power source and energy storage devices, respectively. Two MFCs were placed in series and were parallel connected to supercapacitors after achieving a 1.8 V OCV value. Within the 45 s time interval, two supercapacitors connected in series were changed from 0.46 to 1.2 V. Then, the output of the DC/DC boost converter boosts the voltage of supercapacitors from 1.2 to 3 V, which is capable to drive a blue LED. Consequently, the voltage of supercapacitors dropped from 1.2 to 0.7 V. After the output of the converter was enabled, the blue LED kept glowing for 15 s as shown in the Supplementary Movie. A number of electrolytic capacitors were placed in the circuit, which was able to store charge while the output was enabled; hence, the blue LED was able to glow after the input voltage of the circuit dropped to 0.7 V.

3. Conclusion

In this study, we successfully synthesized the nanoporous TNHs and used them as electrodes in MFCs and SCs. The performance of MFC was optimized by varying the carbonization temperature for preparation of TNHs. TNH-800 as the anode material exhibited a lower resistivity and better *E. coli* adhesion than the other TNHs, whereas TNH-1000 as the cathode material showed a higher ORR activity. The MFC with the TNH-800 anode and TNH-1000 cathode exhibited the highest average power density of 5712.5 mW m^{-2}, which is twice as large as the MFC using CAC electrodes (2998.3 mW m^{-2}). Furthermore, the TNHs were also used as electrode materials for the SCs, with TNH-600 exhibiting the highest specific capacitance of up to 84 F g^{-1} and a good cycling stability. These results demonstrated that the MFC assembled with the TNH anodes and cathodes exhibited considerably higher performance than the MFC using CAC electrodes. As a proof of concept, we additionally assembled a TNH-based MFC-SC system with a DC–DC converter and succeeded to light up a LED for 15 min. Overall, using *T. natans* husks as a raw material for MFC and SC electrodes increases the economic value of the agricultural waste and reduces CO_2 emissions generated during waste disposal, demonstrating the potential of TNH in developing MFCs as a sustainable energy source.

4. Experimental Section

Preparation of TNH: The *T. natans* husks were obtained from Guantian Black Gold in Tainan City, Taiwan. Figure 1b presents the process flow for the synthesis of the TNHs. First, the *T. natans* husks were washed with deionized water, filtered to remove impurities, and dried. The dried *T. natans* husks were activated by a saturated $ZnCl_2$ solution for 24 h at a weight ratio of 1:1. Next, the *T. natans* husks were carbonized in a nitrogen

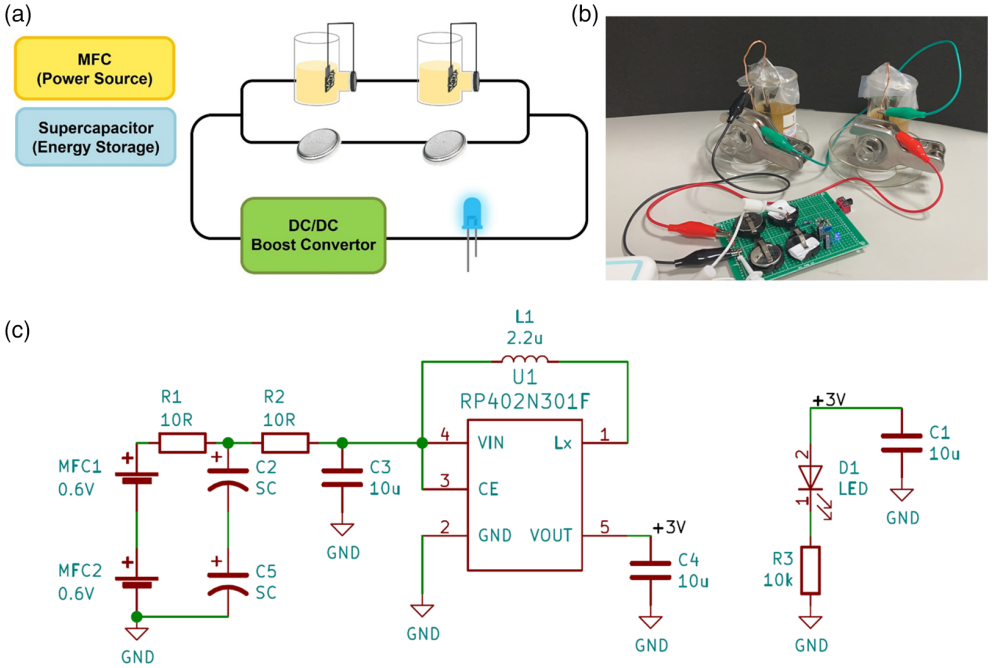


Figure 14. a) Schematic and b) photography of the MFC-SC-LED system; c) schematic of the DC/DC boost converter circuit system.

© 2021 The Authors. Advanced Energy and Sustainability Research published by Wiley-VCH GmbH

atmosphere at 600, 800, and 1000 °C for 2 h. After ball-milling for 24 h, the powder was washed with 1 M HCl to remove $ZnCl_2$ and other impurities. Finally, the sample was cleaned with deionized water until a pH of 7 was reached, followed by drying. The obtained TNHs, including TNH-600 (carbonized at 600 °C), TNH-800 (carbonized at 800 °C), and TNH-1000 (carbonized at 1000 °C), were the experimental groups, while CAC was the control group.

Material Characterization: The surface areas and pore size distributions of the TNH samples were determined with a BET analysis by measuring the N_2 adsorption–desorption isotherms at 77 K. The morphologies of the TNH samples were observed using field-emission SEM (FESEM). The crystallinity of the TNH powders was characterized by XRD with Cu Kα radiation, in which the 2θ angle ranged from 10° to 60°, using $0.02° s^{-1}$steps. The degree of carbonization of the TNH samples was detected by Raman spectroscopy using a 532 nm laser excitation source. XPS using an Al Kα source was used to analyze the elemental components and bonding on the TNH surface. SCA was used to measure the hydrophilicity by using a 2 µL drop of deionized water.

MFC Construction: The MFC was constructed in a 40 mL single chamber with an air-exposed cathode (Figure 1a). The anode was a 1 × 1 cm^2 carbon cloth substrate coated with 15 mg of CAC or TNHs. The active material, carbon black (Super P), and polyvinylidene difluoride (PVDF) were mixed to a weight ratio of 8:1:1 in *n*-methyl-2-pyrrolidone (NMP) solvent and stirred for 24 h. After stirring, the slurry was coated onto a carbon cloth and dried. The cathode was a 2 × 2 cm^2 carbon cloth substrate coated with 40 mg CAC or TNHs active material using the same method as that used for the anode, and the actual working area of the cathode was 2 cm^2. A Nafion 117 membrane was attached to the cathode to separate the two electrodes. LB growth medium (5 × g L^{-1} Bacto Peptone, 10 × g L^{-1} yeast extract, and 10 × g L^{-1} NaCl, adjusted to pH = 7) was used as the nutrient solution for the *E. coli* DH5α growth. A 20 µL aliquot of the *E. coli* DH5α preculture was added to a 40 mL LB solution, and the solution concentration was quantified by OD_{600} ranging from 0.035 to 0.04. Subsequently, it was cultivated for 16 h at 37 °C with shaking at 200 rpm with an anode electrode inside the solution. After cultivation, the culture solution was transferred to a single-chamber device, as shown in Figure 1a.

The anodes were immersed in 25% glutaraldehyde for 3 h at 4 °C after washing with deionized water to observe the distribution of microbes on the TNHs. Next, the anodes were immersed in increasing concentrations of ethanol solutions (i.e., 30%, 50%, 70%, 80%, 90%, and 99.5%) for 15 min each to dehydrate them.[80] Subsequently, the samples were dried using a critical point dryer using CO_2. Finally, the dried TNH anodes were coated with platinum, and the *E. coli* DH5α distribution on the TNH anode was examined by FESEM.

MFC Performance Measurements: The MFC material optimization was divided into two parts. The anode was optimized first, and then the cathode performance with different nanoporous carbons was also measured with the optimized anode. CV was performed using a three-electrode system to study the electron transfer ability and redox reactions of the anode. The CV curves were recorded from −0.8 to 0.8 V at a scan rate of 20 mV s^{-1}. The sheet resistance was detected using four-point probe measurements. LSV was performed in both the anode and cathode tests using a two-electrode system, and was utilized to investigate the power densities and polarization curves by scanning from the OCV to 0 mV at 1 mV s^{-1}. The power density was calculated by multiplying the cell voltage and current density, which were normalized to the working area of the anode. A three-electrode LSV was constructed with Ag/AgCl (25 °C, saturated with KCl solution) as the reference electrode to obtain the three-electrode polarization curves to precisely detect the performance of the cathode. For comparison with other reported MFCs, a polarization curve was also obtained by measuring the closed-circuit voltage with external resistances continuously varying from 5000 to 200 Ω for 20 min for each resistance measurement. The power and current densities were calculated using Ohm's law and were also normalized to the working area of the anode.

RDE Measurement: To measure the ORR activities in RDE, a catalyst-coated substrate was prepared as the catalyst. Absolute ethanol, Nafion solution (5%), and DI water were mixed in the ratio of 2 mg:120 µL:40 µL by ultrasonication for 30 min to form homogenous inks. The working area of the glassy carbon electrode was 0.1962 cm^2 with 7 µL ink, and the electrolyte was phosphate-buffered saline (PBS) with a pH of 7.2. When the electrode was well immersed in the oxygen/nitrogen-saturated PBS solution, it was scanned from 0.6 to −0.6 V at 10 mV s^{-1} at different rotation speeds.[34,46,48,81,82]

SECM Measurement: To study the microscale electrochemical activity differences between the TNHs and CAC, SECM experiments were conducted on a SECM150 (BioLogic) system. A four-electrode setup was adopted, including two platinum wires as the reference and counter electrodes, a catalyst-coated platinum plate as the working electrode, and a 10 µm diameter platinum probe with a fused silica insulating sheath (U-23/10, BioLogic) as the probe working electrode. To prepare the catalyst-coated substrate, the catalyst, absolute ethanol, and Nafion solution (5%) were mixed in the ratio of 2 mg:90 µL:10 µL by ultrasonication for 30 min to form homogenous inks. Ten microliter of TNH-600, TNH-800, TNH-1000, and CAC catalyst inks were drop-cast on each of the four quadrant areas of a platinum plate, as shown in Figure S7, Supporting Information. The electrolyte used for the SECM measurement was a mixture of 0.1 M KCl and 0.1 M $K_3[Fe(CN)_6]$ aqueous solution. The distance between the probe tip and sample surface was controlled to approximately 40 µm by the approaching curve test. A 600 × 600 $µm^2$ area was scanned for each catalyst area. The potentials of the probe and substrate were set at −0.4 and −0.02 V (vs Pt), respectively. The scanning step sizes of both the *X* and *Y* directions were set to 10 µm.

SC Assembly and Analysis: The electrodes were fabricated by mixing 80 wt% active carbon materials (TNH-600, TNH-800, TNH-1000, or CAC), 10 wt% carbon black (super P), and 10 wt% binder (PVDF). Then, several drops of NMP were added to form a homogeneous mixture. The uniform slurry was coated onto graphite paper, which acted as a current collector, and dried overnight at 80 °C to remove the NMP solution. Two identical disk-shaped electrodes (130 mm diameter) were prepared from the dried coated graphite paper and weighed. Finally, the carbon–carbon symmetric SC was assembled as a coin cell. CV and GCD were performed to characterize the electrochemical performance of the SCs using a Biologic VMP3 potentiostat and a Neware battery testing system.

DC/DC Boost Construction: Owing to the nonlinear output voltage characteristic of MFCs, an electric actuator (DC/DC boost converter) is required for further applications. DC/DC boost converters are devices that step up an unregulated low DC input voltage and generate a relatively higher and regulated DC output voltage. In this study, a cost-effective DC/DC boost converter circuit system was constructed, and a schematic of the circuit is shown in Figure 14. This circuit system was powered by the MFCs to drive a blue LED. A discrete DC/DC boost converter integrated circuit (RP402x series, RICOH) was adopted. The input voltage of the circuit system was designed to be 0.8–2.0 V and the output voltage was fixed at 3 V. Two MFCs (MFC1 and MFC2) were placed in series to increase the input voltage of the converter, and further increase the conversion efficiency.[83] To compensate for the nonlinear voltage characteristics of the MFCs, two SCs (C2 and C5) were placed in parallel with the cells.

Supporting Information

Supporting Information is available from the Wiley Online Library or from the author.

Acknowledgements

C.-C.H. and Y.-C.L. contributed equally to this work. This work was financially supported by the Young Scholar Fellowship Program of the Ministry of Science and Technology (MOST) in Taiwan under grant no. MOST 110-2636-E-007-007 to Dr. Han Yi-Chen and by the grant no. MOST 105-2621-M-007-001-MY3 to Dr. Tzu-Yin Liu. It is also supported by the National Tsing Hua University (110Q2730E1). The authors thank the Instrumentation Center at National Tsing Hua University for assisting with

© 2021 The Authors. Advanced Energy and Sustainability Research published by Wiley-VCH GmbH

the electron spectroscopy for chemical analysis and with the X-ray diffraction measurement for structural analysis (MOST 110-2731-M-007-001).

Conflict of Interest

The authors declare no conflict of interest.

Data Availability Statement

Research data are not shared.

Keywords

activated carbon, high power density, microbial fuel cells, *Trapa natans* husks

Received: September 30, 2021
Revised: November 3, 2021
Published online: December 15, 2021

[1] H.-L. Song, Y. Zhu, J. Li, *Arab. J. Chem.* **2019**, *12*, 2236.
[2] M. Rahimnejad, A. A. Ghoreyshi, G. Najafpour, T. Jafary, *Appl. Energy* **2011**, *88*, 3999.
[3] B. E. Logan, J. M. Regan, *Microbial Fuel Cells—challenges And Applications*, ACS Publications Environ. Sci. Technol, **2006**, 40, 5172–5180.
[4] R. Wang, M. Yan, H. Li, L. Zhang, B. Peng, J. Sun, D. Liu, S. Liu, *Adv. Mater.* **2018**, *30*, e1800618.
[5] B. E. Logan, B. Hamelers, R. Rozendal, U. Schröder, J. Keller, S. Freguia, P. Aelterman, W. Vxerstraete, K. Rabaey, *Environ. Sci. Technol.* **2006**, *40*, 5181.
[6] C. Choi, Y. Cui, *Bioresour. Technol.* **2012**, *107*, 522.
[7] J. Yu, *J. Chem. Pharm. Res.* **2014**, *6*, 333.
[8] Y.-H. Hung, T.-Y. Liu, H.-Y. Chen, *ACS Sustain. Chem. Eng.* **2019**, *7*, 16991.
[9] R.-B. Song, C.-E. Zhao, L.-P. Jiang, E. S. Abdel-Halim, J.-R. Zhang, J.-J. Zhu, *ACS Appl. Mater. Interfaces* **2016**, *8*, 16170.
[10] K. Zou, Y. Deng, J. Chen, Y. Qian, Y. Yang, Y. Li, G. Chen, *J. Power Sources* **2018**, *378*, 579.
[11] Y.-C. Liu, Y.-H. Hung, S.-F. Liu, C.-H. Guo, T.-Y. Liu, C.-L. Sun, H.-Y. Chen, *Sustain. Energy Fuels* **2020**, *4*, 5339.
[12] F. Li, D. Wang, Q. Liu, B. Wang, W. Zhong, M. Li, K. Liu, Z. Lu, H. Jiang, Q. Zhao, C. Xiong, *J. Power Sources* **2019**, *412*, 514.
[13] Y.-M. Chen, C.-T. Wang, Y.-C. Yang, W.-J. Chen, *Int. J. Hydrogen Energy* **2013**, *38*, 11131.
[14] Y. Zhang, G. Mo, X. Li, W. Zhang, J. Zhang, J. Ye, X. Huang, C. Yu, *J. Power Sources* **2011**, *196*, 5402.
[15] P. Khare, J. Ramkumar, N. Verma, *Electrochim. Acta* **2016**, *219*, 88.
[16] T. Sharma, A. Mohanareddy, T. Chandra, S. Ramaprabhu, *Int. J. Hydrogen Energy* **2008**, *33*, 6749.
[17] G. Gnana kumar, C. J. Kirubaharan, S. Udhayakumar, C. Karthikeyan, K. S. Nahm, *Ind. Eng. Chem. Res.* **2014**, *53*, 16883.
[18] X. Xie, G. Yu, N. Liu, Z. Bao, C. S. Criddle, Y. Cui, *Energy Environ. Sci.* **2012**, *5*, 6862.
[19] S. Singh, P. K. Bairagi, N. Verma, *Electrochim. Acta* **2018**, *264*, 119.
[20] X. Chen, D. Cui, X. Wang, X. Wang, W. Li, *Biosens. Bioelectron.* **2015**, *69*, 135.
[21] A. Mehdinia, E. Ziaei, A. Jabbari, *Electrochim. Acta* **2014**, *130*, 512.
[22] G. Gnana kumar, C. J. Kirubaharan, S. Udhayakumar, K. Ramachandran, C. Karthikeyan, R. Renganathan, K. S. Nahm, *ACS Sustain. Chem. Eng.* **2014**, *2*, 2283.
[23] Y.-C. Liu, Y.-H. Hung, Sutarsis, C.-C. Hsu, C.-S. Ni, T.-Y. Liu, J.-K. Chang, H.-Y. Chen, *Renew. Energy* **2021**, *171*, 87.
[24] B. Bian, D. Shi, X. Cai, M. Hu, Q. Guo, C. Zhang, Q. Wang, A. X. Sun, J. Yang, *Nano Energy* **2018**, *44*, 174.
[25] F. Rodríguez-reinoso, *Carbon* **1998**, *36*, 159.
[26] C. Santoro, M. Kodali, N. Shamoon, A. Serov, F. Soavi, I. Merino-Jimenez, I. Gajda, J. Greenman, I. Ieropoulos, P. Atanassov, *J. Power Sources* **2019**, *412*, 416.
[27] F.-Y. Zheng, R. Li, S. Ge, W.-R. Xu, Y. Zhang, *J. Power Sources* **2020**, *446*, 227356.
[28] M. V. Kannan, G. Gnana Kumar, *Biosens. Bioelectron.* **2016**, *77*, 1208.
[29] M. Zhong, C. Ren, D. Fang, C. Lv, K. Li, *J. Electroanal. Chem.* **2020**, *878*, 114570.
[30] X. Zhang, X. Guo, Q. Wang, R. Zhang, T. Xu, P. Liang, X. Huang, *J. Mater. Chem. A* **2020**, *8*, 10772.
[31] X. Zhang, X. Xia, I. Ivanov, X. Huang, B. E. Logan, *Environ. Sci. Technol.* **2014**, *48*, 2075.
[32] F.-Y. Zheng, R. Li, S. Ge, W.-R. Xu, Y. Zhang, *J. Power Sources* **2020**, *446*, 227356.
[33] M. Zhong, C. Ren, D. Fang, C. Lv, K. Li, *J. Electroanal. Chem.* **2020**, *878*, 114570.
[34] M. Kodali, S. Herrera, S. Kabir, A. Serov, C. Santoro, I. Ieropoulos, P. Atanassov, *Electrochim. Acta* **2018**, *265*, 56.
[35] C. Santoro, M. Kodali, S. Kabir, F. Soavi, A. Serov, P. Atanassov, *J. Power Sources* **2017**, *356*, 371.
[36] B. Ge, K. Li, Z. Fu, L. Pu, X. Zhang, *Bioresour. Technol.* **2015**, *195*, 180.
[37] H. Yuan, Y. Hou, Z. Wen, X. Guo, J. Chen, Z. He, *ACS Appl. Mater. Interfaces* **2015**, *7*, 18672.
[38] J. Huang, H. Feng, Y. Jia, D. Shen, Y. Xu, *Water Sci. Technol.* **2019**, *80*, 1399.
[39] Y. Sun, Z. Zhang, Y. Sun, G. Yang, *Int. J. Agric. Biol. Eng.* **2020**, *13*, 207.
[40] B. Zhang, Z. Wen, S. Ci, S. Mao, J. Chen, Z. He, *ACS Appl Mater Interfaces* **2014**, *6*, 7464.
[41] T. M. Huggins, J. J. Pietron, H. Wang, Z. J. Ren, J. C. Biffinger, *Bioresour. Technol.* **2015**, *195*, 147.
[42] F. Shahbazi Farahani, B. Mecheri, M. R. Majidi, E. Placidi, A. D'Epifanio, *Carbon* **2019**, *145*, 716.
[43] M. R. Majidi, F. Shahbazi Farahani, M. Hosseini, I. Ahadzadeh, *Bioelectrochemistry* **2019**, *125*, 38.
[44] S. B. Velasquez-Orta, T. P. Curtis, B. E. Logan, *Biotechnol. Bioeng.* **2009**, *103*, 1068.
[45] V. J. Watson, B. E. Logan, *Electrochem. Commun.* **2011**, *13*, 54.
[46] Y. Liu, Y.-S. Fan, Z.-M. Liu, *Chem. Eng. J.* **2019**, *361*, 416.
[47] B. Mecheri, R. Gokhale, C. Santoro, M. A. Costa de Oliveira, A. D'Epifanio, S. Licoccia, A. Serov, K. Artyushkova, P. Atanassov, *ACS Appl. Energy Mater.* **2018**, *1*, 5755.
[48] K. Lv, H. Zhang, S. Chen, *RSC Adv.* **2018**, *8*, 848.
[49] C. Santoro, A. Serov, R. Gokhale, S. Rojas-Carbonell, L. Stariha, J. Gordon, K. Artyushkova, P. Atanassov, *Appl. Catal., B* **2017**, *205*, 24.
[50] X. Zeng, D. Liu, S. Wang, S. Liu, X. Cai, L. Zhang, R. Zhao, B. Li, F. Kang, *ACS Appl. Mater. Interfaces* **2020**, *12*, 37047.
[51] D. Liu, Q. Yu, S. Liu, K. Qian, S. Wang, W. Sun, X.-Q. Yang, F. Kang, B. Li, *J. Phys. Chem. C* **2019**, *123*, 12797.
[52] S. Liu, D. Liu, S. Wang, X. Cai, K. Qian, F. Kang, B. Li, *J. Mater. Chem. A* **2019**, *7*, 12993.
[53] S. R. Catarelli, D. Lonsdale, L. Cheng, J. Syzdek, M. Doeff, *Front. Energy Res.* **2016**, *4*.
[54] E. Ventosa, W. Schuhmann, *Phys. Chem. Chem. Phys.* **2015**, *17*, 28441.
[55] J. Zhang, T. Zhu, J. Lang, W. Fu, F. Li, *Curr. Opin. Electrochem* **2020**, *22*, 178.

© 2021 The Authors. Advanced Energy and Sustainability Research published by Wiley-VCH GmbH

[56] L. Huang, Z. Li, Y. Lou, F. Cao, D. Zhang, X. Li, *Materials* **2018**, *11*, 1389.
[57] T. Kai, C. G. Zoski, A. J. Bard, *Chem. Commun.* **2018**, *54*, 1934.
[58] D. Polcari, P. Dauphin-Ducharme, J. Mauzeroll, *Chem. Rev.* **2016**, *116*, 13234.
[59] A. Preet, T.-E. Lin, *Catalysts* **2021**, *11*, 594.
[60] D. Filotás, B. M. Fernández-Pérez, L. Nagy, G. Nagy, R. M. Souto, *J. Electroanal. Chem.* **2021**, *895*, 115538.
[61] F. D. Mayer, P. Hosseini-Benhangi, C. M. Sánchez-Sánchez, E. Asselin, E. L. Gyenge, *Commun. Chem.* **2020**, *3*, 155.
[62] Y. Liang, J. H. K. Pfisterer, D. McLaughlin, C. Csoklich, L. Seidl, A. S. Bandarenka, O. Schneider, *Small Methods* **2019**, *3*, 1800387.
[63] A. Dobrzeniecka, A. R. Zeradjanin, J. Masa, M. Blicharska, D. Wintrich, P. J. Kulesza, W. Schuhmann, *Catal. Today* **2016**, *262*, 74.
[64] S. Cannan, J. Cervera, R. J. Steliaros, E. Bitziou, A. L. Whitworth, P. R. Unwin, *Phys. Chem. Chem. Phys.* **2011**, *13*, 5403.
[65] C. Lefrou, R. Cornut, *ChemPhysChem* **2010**, *11*, 547.
[66] P. Bertoncello, *Energy Environ. Sci.* **2010**, *3*, 1620.
[67] X. Chen, R. Paul, L. Dai, *Natl. Sci. Rev.* **2017**, *4*, 453.
[68] Z. Yang, J. Ren, Z. Zhang, X. Chen, G. Guan, L. Qiu, Y. Zhang, H. Peng, *Chem. Rev.* **2015**, *115*, 5159.
[69] M. Thommes, K. Kaneko, A. V. Neimark, J. P. Olivier, F. Rodriguez-Reinoso, J. Rouquerol, K. S. Sing, *Pure Appl. Chem.* **2015**, *87*, 1051.
[70] J. Feng, R. Tang, X. Wang, T. Meng, *ACS Appl. Energy Mater.* **2021**, *4*, 5230.
[71] T. Ungar, J. Gubicza, G. Ribarik, C. Pantea, T. W. Zerda, *Carbon* **2002**, *40*, 929.
[72] K. Ray, R. L. McCreery, *Anal. Chem.* **1997**, *69*, 4680.
[73] A. Heidari, H. Younesi, A. Rashidi, A. A. Ghoreyshi, *Chem. Eng. J.* **2014**, *254*, 503.
[74] P. Yang, N. Huang, Y. Leng, Z. Yao, H. Zhou, M. Maitz, Y. Leng, P. Chu, *Nucl. Instrum. Methods Phys. Res. B: Beam Interact. Mater. At.* **2006**, *242*, 22.
[75] X. Lu, D. Wang, L. Ge, L. Xiao, H. Zhang, L. Liu, J. Zhang, M. An, P. Yang, *New J. Chem.* **2018**, *42*, 19665.
[76] J. Quílez-Bermejo, M. Melle-Franco, E. San-Fabián, E. Morallón, D. Cazorla-Amorós, *J. Mater. Chem. A* **2019**, *7*, 24239.
[77] A. Zhao, J. Masa, W. Schuhmann, W. Xia, *J. Phys. Chem. C* **2013**, *117*, 24283.
[78] Y. Hirotoshi, N. Haruka, N. Fumihiro, *J. Phys. Chem. C* **2007**, *111*, 227.
[79] M. O. Ilomuanya, B. Nashiru, N. D. Ifudu, C. I. Igwilo, *J Microsc Ultrastruct* **2017**, *5*, 32.
[80] P. Zhang, J. Liu, Y. Qu, J. Zhang, Y. Zhong, Y. Feng, *J. Power Sources* **2017**, *361*, 318.
[81] B. Mecheri, R. Gokhale, C. Santoro, M. A. Costa de Oliveira, A. D'Epifanio, S. Licoccia, A. Serov, K. Artyushkova, P. Atanassov, *ACS Appl. Energy Mater.* **2018**, *1*, 5755.
[82] C. Santoro, A. Serov, R. Gokhale, S. Rojas-Carbonell, L. Stariha, J. Gordon, K. Artyushkova, P. Atanassov, *Appl. Catal., B* **2017**, *205*, 24.
[83] J. Kan, S. Xie, Y. Wu, Y. Tang, Z. Yao, R. Chen, *IEEE Trans. Ind. Electron.* **2015**, *62*, 5480.

© 2021 The Authors. Advanced Energy and Sustainability Research published by Wiley-VCH GmbH